Published in final edited form as:
IEEE Trans Image Process. 2014 March ; 23(3): 1340–1351. doi:10.1109/TIP.2014.2300751.

A Complete System for Automatic Extraction of Left Ventricular Myocardium From CT Images Using Shape Segmentation and Contour Evolution

Liangjia Zhu,
Department of Computer Science, Stony Brook University, Stony Brook, NY 11794 USA

Yi Gao,
Department of Electrical and Computer Engineering, Comprehensive Cancer Center, University of Alabama at Birmingham, Birmingham, AL 35294 USA

Vikram Appia,
School of Electrical and Computer Engineering, Georgia Institute of Technology, Atlanta, GA 30303 USA

Anthony Yezzi,
School of Electrical and Computer Engineering, Georgia Institute of Technology, Atlanta, GA 30303 USA

Chesnal Arepalli,
Department of Radiology, Emory University, Atlanta, GA 30322 USA

Tracy Faber,
Department of Radiology, Emory University, Atlanta, GA 30322 USA

Arthur Stillman, and
Department of Radiology, Emory University, Atlanta, GA 30322 USA

Allen Tannenbaum [Fellow, IEEE]
Department of Computer Science and Department of Applied Mathematics/Statistics, Stony Brook University, Stony Brook, NY 11794 USA

Liangjia Zhu: liangjia.zhu@stonybrook.edu; Yi Gao: gaoyi@uab.edu; Vikram Appia: vikram.appia@gatech.edu; Anthony Yezzi: ayezzi@ece.gatech.edu; Chesnal Arepalli: carepal@emory.edu; Tracy Faber: tfaber@emory.edu; Arthur Stillman: aestill@emory.edu; Allen Tannenbaum: allen.tannenbaum@stonybrook.edu

Abstract

The left ventricular myocardium plays a key role in the entire circulation system and an automatic delineation of the myocardium is a prerequisite for most of the subsequent functional analysis. In this paper, we present a complete system for an automatic segmentation of the left ventricular myocardium from cardiac computed tomography (CT) images using the shape information from images to be segmented. The system follows a coarse-to-fine strategy by first localizing the left ventricle and then deforming the myocardial surfaces of the left ventricle to refine the segmentation. In particular, the blood pool of a CT image is extracted and represented as a triangulated surface. Then, the left ventricle is localized as a salient component on this surface using geometric and anatomical characteristics. After that, the myocardial surfaces are initialized from the localization result and evolved by applying forces from the image intensities with a constraint based on the initial myocardial surface locations. The proposed framework has been validated on 34-human and 12-pig CT images, and the robustness and accuracy are demonstrated.

Index Terms

Myocardium segmentation; left ventricle; shape segmentation; contour evolution

I. Introduction

Cardiovascular diseases are the leading causes of death in the world [1]. The diagnosis and treatment of these diseases may rely on different cardiac image modalities. No matter what modality is used, the clinical importance of delineating the myocardial boundaries is the highest [2]. Though this tedious task can be done manually in about 20 minutes with sophisticated interactive segmentation tools, the intra- and inter-observer variability is still inevitable [3]. The automatic segmentation methods with high accuracy are attractive because of the previous mentioned reasons. In this paper, we will focus on the segmentation of the left ventricular myocardium from computed tomography (CT) images.

A. Related Work

The main challenges in extracting the myocardium include large shape variability within cardiac cycles and between different patients, and weak edges between epicardium and heart fat or soft tissues. To get an accurate and robust segmentation, model-based methods have become dominant in this research [2]. Heart models are commonly used to represent the geometric or intensity features of the heart, and they are applied either explicitly or implicitly for segmentation. In the first type of methods, models created off-line are fitted to images for segmentation. For example, active shape models (ASMs) [4] build a statistical shape model from a set of aligned shapes by using the principal component analysis (PCA) technique, and have been used for left ventricle segmentation [5], [6]. Active appearance models (AAMs) extend this idea by incorporating gray level information [7] and have been used in segmenting the left and right ventricles from MR images [8]. The deformations allowed in the parametric models such as ASMs and AAMs are confined to the shape space where the heart models are embedded. A more sophisticated way of representing the shape space is by using 3D diffusion wavelets [9], which encode shape variations hierarchically. Using deformable models provides a flexible way to incorporate shape priors that are capable of adapting to local image content. For example, Ecabert *et al.* [10] modeled the whole heart as a multi-compartment, triangulated surface. The local adaptation was achieved by progressively optimizing the piecewise affine transformations of this model to match image boundaries. In [11], a mean shape of the heart was fitted to an image by estimating similarity transformations, which was then deformed to match image boundaries with the help of landmark points on the interventricular septum. Instead of deforming a pre-aligned model, atlas-based methods use shape information implicitly by directly registering each atlas image to a target image. Then, either the labels from multiple atlases are fused [12] or one single registered atlas is deformed [13] to extract the heart region. Model-free methods have also been widely used to explore the characteristics of heart geometry or intensity distribution from other perspectives. For example, the geometric and intensity features in the myocardial region were learned by using a random forests method for delineating the myocardium [14]. For a comprehensive literature review of heart segmentation, see [2], [3] and references therein.

Active contour models have been widely used in medical image segmentation because of their flexibility and robustness. In these models, energy functionals are commonly defined over image features such as edges [15], [16], region statistics [17], local characteristics [18], [19], and a combination of edges and regions [20], [21], which are optimized by using gradient descent techniques. Prior information can be incorporated as well to restrict the optimization space. For example, in [22], an active contour model was evolved in the shape space of the left ventricle obtained by applying the PCA to manually segmented images. Local variations may be captured by decomposing images into different regions using prior information for ventricles segmentation [23], [24] or by modeling a shape prior using pixel-wise stochastic level sets to extract the endocardium [25]. A shape constraint was also employed to control the search space of the myocardial contours between two consecutive image slices [26]. Coupled active contours have been proposed with distance constraints between contours for myocardium extraction [27], cortex segmentation [28], and cell tracking [29].

One important but less studied topic is how to locate the heart initially, especially for these methods using deformable models, which tend to get stuck in undesirable local extrema when started without a good initialization. Typically, the geometric features of the heart are used for localization. In [26], the endocardium was initialized by searching for a circular structure in a blood pool mask obtained via thresholding. Similar empirical rules were used to identify the left ventricle cavity [30]. To capture a more generic shape of the heart, the generalized Hough transform was utilized for heart detection [10]. In [11], the localization was achieved by searching for a similarity transformation in a hierarchical way. Atlas-based registration has also been used for coarse initialization [9], [13].

One fact that has been ignored in the literature for the localization is that the left ventricle is a salient component on the heart surface. This is where the shape decomposition/segmentation technique may be utilized to cluster the surface into *meaningful* components based on some given criteria as in computer graphics and geometric modeling [31], [32]. For example, a surface may be hierarchically decomposed into regions of deep concavities by using fuzzy clustering and graph partition techniques [33]. Prominent feature points [34] have also been used to cluster a surface into meaningful regions. Applications of shape segmentation in medical imaging can be found in heart modeling from images [35] and aneurysm neck detection on vessel surfaces [36]. Active contour models have been applied as well on surfaces to refine coarse segmentations [37] or extract objects of interest [38]. Among the few applications of the shape decomposition techniques to cardiac image segmentation, the *narrowing* of vessels around the left atrium was detected by merging local features based on given criteria to extract the left atrium [39]. As for the left ventricle localization, the region near the left ventricle is much more recognizable from the heart surface than from the volumetric data, which can be identified by a deep concave contour.

B. Method Overview and Our Contributions

In this work, we present a complete system for automatically extracting the myocardium from cardiac CT images without using training images. A coarse-to-fine strategy, consisting of global localization and local deformations, is used for the myocardium segmentation. The flowchart of the proposed method is shown in Fig. 1.

Before starting the localization step, the heart surface is approximated by the blood pool surface. Then, the apex point of the left ventricle on this surface is detected by using the relative orientation of ventricles with respect to the physical coordinate system of a CT image. The left ventricle is automatically detected by examining the distribution of the level sets starting from the apex point, which is further refined by performing the geometric active contour model on the blood pool surface. This contour decomposes the surface into two parts, and the one contains the apex point is chosen as the initial endocardial surface. Once the endcoardial surface is located, its corresponding mask is obtained via rasterization. Then, a variational region-growing method [40] is used to extract the initial epicardial surface based on the endocardium segmentation. Finally, these two surfaces are refined by employing an active contour model with a shape constraint, and the myocardium is obtained by extracting voxels between these surfaces.

The contributions of the proposed method are as follows:

1: we utilize the shape segmentation technique for localizing the left ventricle. Unlike other methods that only use low level information from voxels, our method captures a global geometric characteristic of the left ventricle that agrees with our visual perception. Hence, it is not sensitive to such issues as shape variability and changes of volume coverage. Note that, as an initialization step, the proposed method can be easily incorporated into other model-based frameworks.

2: we use a variational region-growing method to locate the epicardial surface given the segmentation of the endocardial surface. Then the localized endocardial and epicardial surfaces are employed as a constraint for the final segmentation. In this formulation, the shape variability is naturally handled and incorporated into our system without using training images. In addition, instead of simply imposing a constraint on the point-wise distance between two contours [28], the one used in our model is a surface-wise restriction that uses a distance field for guiding contour evolution process.

Therefore, the overall system is complete in that all the active contour models involved are initialized automatically and robustly, other than in those systems that active contours are either used as a single component or initialized manually.

The rest of this paper is organized as follows: Section II describes the details of left ventricle localization. Section III introduces the active contour model with a shape constraint obtained from the localization results. The robustness and accuracy of the proposed method are reported in Section IV. Finally, Section V concludes this paper.

II. Left Ventricle Localization

Assume that the orientation of a CT image is given and intensity contrast exists between blood pool and myocardium. The localization of the left ventricle is determined via searching for a deep concave boundary on the blood pool surface as follows.

A. Extract Blood Pool Surface

The extraction of the blood pool surface is carried out by a few mature techniques in the computer vision and graphics: since CT images have calibrated gray levels, the source image is thresholded to highlight the blood pool region. Then, the morphological opening operator is applied to remove noisy arteries and cut spines that may be residing in the same connected component of the heart. After that, the largest connected component is chosen and triangulated to get the blood pool surface.

B. Detect Apex Point

Suppose the coordinate system of the source image is Left-Posterior-Inferior (LPI) as shown in Fig. 2. In this system, the XYZ coordinates trace from left to right, posterior to anterior, and inferior to superior. Even though the long axis of pig and human heart has different orientations [41], the directions of *left* and *right* are clearly defined from the inferior view. The apex point is one salient feature that can be used to locate the left ventricle. Its location is determined as follows: 1) estimate the orientation of ventricles; 2) search for the left ventricle apex, which is the *left* tip point with respect to the estimated orientation.

To estimate the orientation of ventricles, the convex hull of the blood pool surface M_{bp} is first constructed. Let $K(\tilde{p})$ be the Gaussian curvature at each vertex $\tilde{p}$ of the convex hull. The vertices used for estimating the ventricle orientation are selected as

$$V_{ch}(\tilde{p})=\{\tilde{p}|K(\tilde{p})>\mu_K+\sigma_K \cap y(\tilde{p})>t_y\}, \quad (1)$$

where μ_K and σ_K are the mean and standard deviation of $K(\tilde{p})$, and a threshold t_y defines the region of interest for the ventricles, which was empirically set as $t_y = y_{min} + 0.5(y_{max} - y_{min})$ to select points in the top half of the source image in the Y direction. Then, all points $\tilde{p} \in V_{ch}$ are translated as $\tilde{p}_s = \tilde{p} - \mu_{bp}$, where μ_{bp} is the centroid of M_{bp}. The PCA technique is utilized to find the principal component of these translated points $\tilde{p}_s$ as the orientation of the ventricles, denoted by **H**. The positive direction is chosen so that **H** has negative component in the Y direction. A plane L_O passing through μ_{bp} with normal $\mathbf{N} = \mathbf{Z} \times \mathbf{H}$ defines a reference plane such that the left ventricle points are mainly above the plane and otherwise for the right ventricle.

Let $\lambda_{max} \in \mathbb{R}$ *s.t.* $\lambda_{\max} = \max(p_s \cdot \mathbf{H})$. A reference point is defined as $p_{rf} = \mu_{bp} + \lambda_{max} \mathbf{H}$. A constraint region-labeling process is employed to search for a neighborhood of the left ventricle apex. First, the corresponding points of V_{ch} on surface M_{bp} are sorted in an ascending order based on their distance to p_{rf}, which is denoted by $\{p_j\}$, $j = 1 \cdots n_{ch}$, where n_{ch} is the cardinality of the set V_{ch}. Then, the distance field starting from p_1 is constructed using the fast marching method [42]. All points with their distances smaller than a threshold

t_n are labeled as 1. After that, the unlabeled point with the smallest index in $\{p_j\}$ is checked. If its distance to p_{rf} is smaller than the maximum distance between labeled points and p_{rf}, then the point is selected to start the labeling process again and the points within the range of t_n are labeled as 2. Let μ_1 and μ_2 be the centroids of these two labeled regions, respectively. The region with a larger projection $(\mu_i - \mu_{bp}) \cdot \mathbf{N}$, $i = 1, 2$, is selected as a neighborhood N_{apx} around the left ventricle apex. If only one labeled region is found, it is automatically selected as N_{apx}. Finally, the point in N_{apx} with the largest projection in $\mathbf{N}$ direction is selected as the apex point.

An illustration of the apex detection process is shown in Fig. 3.

C. Identify Cut Contour

A two-step segmentation strategy is used to identify the left ventricle by searching for a *cut contour* on M_{bp}.

1) Find an Initial Cut Contour—The initial cut contour, denoted by C_0, is determined based on the distance field starting from p_{apx}. Sampling this distance field evenly at an interval of 2 mm gives its isocontours/level-sets as shown in Fig. 4(a). The total length of each isocontour increases gradually and then drops slightly as it is traveling along the left ventricle. After that, it goes up first and then drops rapidly as it is propagating to the right ventricle and other regions (see Fig. 4(b)). Thus, the total length of an isocontour at distance d may be modeled by

$$h(d,\tilde{d})=\begin{cases} c_0+c_1d+c_2d^2 & \text{if}\, d\le\tilde{d} \\ ae^{-\frac{(d-\mu)^2}{2\sigma^2}} & \text{if}\, d>\tilde{d}, \end{cases} \quad (2)$$

where $\tilde{d}$ is serving as a turning point for these changes. Let (d_i, l_i), $i = 1 \cdots n$, be a pair of a sampled distance and its corresponding isocontour length, where n is the number of samples over the distance field. Then, choose the isocontour at d_{j^*} as the initial cut contour, where j^* is determined by searching for the optimal turning point that minimizes the least-squares fitting error,

$$J^*=\arg\min_{j}\left(\arg\min_{c_0,c_1,c_2}\sum_{i=1}^{j}(h(d_i,d_j)-l_i)^2+\arg\min_{a,\mu,\sigma}\sum_{i=j+1}^{n}(\log h(d_i,d_j)-\log l_i)^2\right) \quad (3)$$

Here, d_j is a sampling point serving as a trial turning point. The optimal turning point d_{j^*} is obtained by exhausting all elements in $\{d_j\}$, $j = 1 \cdots n$. An illustration of the model fitting process described above is shown in Fig. 4.

2) Refine the Cut Contour—The geometric active contour model [15], [16] is utilized to refine the initial cut contour C_0. Suppose a contour on the surface M_{bp} is represented by the zero level set of a function $U : M \to \mathbb{R}$ with $U(C(p, t)) = 0$, where $C(p, t)$ is a family of contours on M. Let $g : M_{bp} \to \mathbb{R}^+$ be a positive function that attracts an active contour to a conceptually desired boundary [37], defined as

$$g(p)=\frac{1}{1+(|\kappa(p)|/S)^2}, \quad (4)$$

where $\kappa(p)$ is the mean curvature at p, and S is a constant for a scaling to enhance the concave regions so that the values of $g(p)$ for such regions are not overwhelmed by those of other regions. In our implementation, $S = 0.01$ was used in all the experiments. As in [37], κ is set to zero if it is positive. Then, the geometric active contour model on the surface M_{bp} is formulated in the level set framework as

$$E(U)=\int_{M_{bp}} g(p)\delta(U(p))|\nabla_{M_{bp}}U(p)|dp, \quad (5)$$

where $\delta(U)$ is the Dirac delta function. The energy $E(U)$ evaluates a weighted contour length. Similar as in $\mathbb{R}^n$, the gradient descent flow of $E(U)$ is

$$\begin{cases} U_t=|\nabla_{M_{bp}}U|\nabla_{M_{bp}}\cdot\left(g(p)\frac{\nabla_{M_{bp}}U}{|\nabla_{M_{bp}}U|}\right) \\ \frac{\partial U}{\partial \vec{n}}|_{\partial M_{bp}}=0 \\ U(0)=U(C_0), \end{cases} \quad (6)$$

where ∂M_{bp} is the boundary of M_{bp} and $\vec{n}$ is the intrinsic outward normal of ∂M_{bp}. Here, $\nabla_{M^{bp}}$ is the del operator on M_{bp}. This flow drives a contour to segment desired boundaries while minimizing the weighted contour length. In particular, it moves a contour on M_{bp} by its geodesic curvature when $g = 1$, which produces the contour of the shortest length.

Numerically, a narrow band method is employed to solve Equation (6). The main steps are summarized as follows.

Algorithm

Narrow band for Geometric Active Contour

```
1  Initialize the level set function $U$ with $C_0$.
2  Construct a narrow band $\Omega_{M^{bp}}$ around the current contour on $M_{bp}$.
3  Update $U$ in $\Omega_{M^{bp}}$, according to
       $U(p,t+1)=U(p,t)+dt\left(|\nabla_{M_{bp}}U|\nabla_{M_{bp}}\cdot\left(g\frac{\nabla_{M_{bp}}U}{|\nabla_{M_{bp}}U|}\right)\right)_{(p,t)}$,   (7)
   where $dt$ is the time step in discretizing $U$.
4  Find the new zero level set of $U$ to update the contour $C$.
5  Repeat steps 2–4 until it converges or reaches the maximum number of iterations.
```

In step 1, U is realized as the signed distance function from C_0, which decomposes M_{bp} into several regions. The sign of U is positive in the region that contains the apex point. The fast marching method is used to build $\Omega_{M^{bp}}$ from C_0 with a threshold φ_{max} to control the size of the narrow band.

Step 3 requires numerical approximations for gradient and divergence operators on a surface. The discretization schemes of [38] are adopted because they naturally capture the geometric properties of surfaces. The surface M_{bp} is represented by a triangle mesh as $M_{bp}=\{V=\{p_i\}_{i=1}^{N}, T=\{T_k\}_{k=1}^{L}\}$, where $p_i \in \mathbb{R}^3$ is the ith vertex and T_k represents the kth triangle. The surface gradient and divergence operators at a vertex are approximated by taking the weighted average of the discretized operators over the first-ring neighbors of the vertex.

Let $f = \{f(p_1), f(p_2), f(p_3)\}$ be a function and $\mathbf{V} = \{\mathbf{V}(p_1), \mathbf{V}(p_2), \mathbf{V}(p_3)\}$ a vector field defined at each vertex. For any point p inside T_k, the values of f and $\mathbf{V}$ can be interpolated as

$$\begin{cases} p=\chi^1(p_1-p_3)+\chi^2(p_2-p_3)+p_3 \\ f(p)=\chi^1(f(p_1)-f(p_3))+\chi^2(f(p_2)-f(p_3))+f(p_3) \\ \mathbf{V}(p)=\chi^1(\mathbf{V}(p_1)-\mathbf{V}(p_3))+\chi^2(\mathbf{V}(p_2)-\mathbf{V}(p_3))+\mathbf{V}(p_3) \end{cases} \quad (8)$$

where $(\chi^1, \chi^2, 1-\chi^1-\chi^2)$ is the barycentric coordinate of T_k. Here, $\chi = (\chi^1, \chi^2)$ defines a local coordinate system for M_{bp}. Then the approximations of these two operators are

$$\nabla_M f(p_i)=\frac{1}{\sum_l Area(T_l)}\sum_l Area(T_l)\nabla_{T_l} f(p_i) \quad (9)$$

$$\nabla_M \cdot \mathbf{V}(p_i)=\frac{1}{\sum_l Area(T_l)}\sum_l Area(T_l)\nabla_{T_l} \cdot \mathbf{V}(p_i), \quad (10)$$

where l traces through all triangles in the first ring of the vertex p_i to average the discretized operators at each vertex (see Appendix for details). Typically, the maximum narrow band width is set as $\varphi_{max} = \min(10, 4l_{max})$ mm, where l_{max} is the length of the longest edge on M_{bp} and 10 mm is about 10% of the maximum distance from the apex point to a turning point (see Section IV-B), such that there is enough support to compute the gradient and divergence operators. The time step of $dt = 1$ was used in our implementation.

In step 4, a new zero level set is obtained from U. The algorithm stops either when the contour stops evolution or the maximum number of iterations is reached.

To reduce the effect of local noise [see Fig. 5(b)], the contour evolution process described above are applied twice. In the first round, set $g = 1$ so that it shortens the initial contour by its geodesic curvature flow. Then, the feature function defined in Equation (4) is used to refine the contour so that it stops at locally concave locations. Finally, the endocardial surface, denoted by M_{endo}, is identified by the cut contour that separates the endocardial surface from other regions on M_{bp}. An illustration of the process for localizing the left ventricle is shown in Fig. 5.

III. Myocardium Wall Segmentation

The endocardial surface indicates the location of the left ventricle, which is rasterized to get its 3D mask $\tilde{I}_{endo}$ for refinement. Instead of simply dilating $\tilde{I}_{endo}$ for approximating the epicaridal mask $\tilde{I}_{epi}$, a variational region-growing model [40] is used by taking an outward neighborhood of $\tilde{I}_{endo}$ as the seed region. After that, a localized region-based active contour model is utilized with a shape constraint imposed by these initial masks to refine the myocardial segmentation.

A. Initialize the Endocardial and Epicardial Masks

The surface M_{endo} is closed via triangulating the points along the cut contour C_{cut}. Here, M_{endo} is still used to denote the closed surface. $\tilde{I}_{endo}$ is created by rasterizing M_{endo} with the same origin and resolution as the source image I. To remove noise and papillary muscles, the convex hull of M_{endo} is computed and set as a ROI for performing the morphological closing operation on $\tilde{I}_{endo}$. The size of the structure element for the closing operator depends on the radii of the papillary muscles, which was empirically set as 3 mm.

One way of initializing the epicardial mask is by dilating the endocardium to a given distance. This works well for the myocardial wall with a nearly uniform thickness. Here, we propose another way to initialize $\tilde{I}_{epi}$. Similar as in the dilation-based methods, a distance field from $\tilde{I}_{endo}$ is computed and a small strip-region that lies between d_{in} and d_{out} away is chosen as the seed region for the epicardial mask. Typically, the values are set to $d_{in} = 2$ mm and $d_{out} = 4$ mm. The blood pool voxels are excluded from this region. Given the seed region of the epicardial mask, the robust-statistics-based energy functional [40] is defined as

$$E_{\mathrm{RS}}(\Phi)=\int_{\Omega}p(\boldsymbol{f}(x))H(\phi(x))dx+\lambda_{\mathrm{RS}}\int_{\Omega}\delta(x)|\nabla\phi(x)|dx, \quad (11)$$

where φ is the signed distance function from $\tilde{I}_{epi}$ and H is the Heaviside function. Here, $p(\boldsymbol{f}(x))$ is the probability density function of a feature vector $\boldsymbol{f}(x)$ that evaluates the intensity median, inter-quartile range, and median absolute deviation at point x, respectively, where $p(\boldsymbol{f}(x))$ is learned from the seed region intensities. The first term in Equation (11) measures the intensity homogeneity inside the contour, and the second term is the length of the contour that controls the smoothness of the final result. In implementation, λ_{RS} was empirically set as $\lambda_{RS} = 0.2$.

The myocardial masks $\tilde{I}_{epi}$ and $\tilde{I}_{end}$ provide a good localization of the epicardium and endocardium, which impose a shape constraint for local refinement, especially on regions of low contrast or poor edges.

B. Evolve Active Contours With a Shape Constraint

Given a mask image $\tilde{I} \in \{\tilde{I}_{endo}, \tilde{I}_{epi}\}$, a feature function $g : \mathbb{R} \to \mathbb{R}^{+}$ is defined over its signed distance function φ as

$$\tilde{g}(\tilde{\phi})=(d_{max}-d_{min})\left(1+exp\left(-\frac{|\tilde{\phi}|-\beta}{\alpha}\right)\right)^{-1}+d_{min}. \quad (12)$$

Here, $g(\tilde{\varphi})$ is a modified sigmoid function, where α and β define the shape and width of the function, respectively, while d_{max} and d_{min} control the range of this function (see Section IV-B for details).

Then, the energy functional for refining the mask images is designed as

$$E(\phi)=\int_{\Omega_x}\delta(\phi(x))\int_{\Omega_y}B(x,y)F(I(y),\phi(y))dydx+\lambda_{\mathrm{LG}}\int_{\Omega}\tilde{g}(\tilde{\phi}(x))\delta(x)|\nabla\phi(x)|dx, \quad (13)$$

where $B(x, y)$ is a ball of radius r centered at x, and $F(I(y), \varphi(y))$ is a generic internal energy term defined over Ω. In this work, the Chan-Vese energy [17] was used for $F(I(y), \varphi(y))$. The first term in Equation (13) is a localized region-based energy [21]. The second term is essentially the geometric active contour energy [15], [16] using the feature image $\tilde{g}$ to prevent the contour from evolving far from its initial location.

The sparse level set method [43] was used to implement the active contour model for its efficiency. In particular, the upwind scheme was used in discretizing $|\nabla(\cdot)|$ (see [44] for details). The refinement of the endocardial and epicardial masks were performed separately. In initializing the epicardial mask, a parameter d_w was used to control the maximum distance allowed in the region-growing process. This parameter is related to the average thickness of the myocardial wall, which typically ranges from 6 to 16 mm [3]. In our implementation, d_w was empirically set as d_w = 16 mm, and r = 4 mm was used for the radius of $B(x, y)$. See Section IV-B for details.

C. Extracting the Myocardial Wall

The myocardial wall is defined as the volume between the endocaridal and epicardial masks. Note that the contour evolution process returns closed masks. To extract a complete myocardial wall, the voxels inside the blood pool need to be removed [seed Fig. 6(d)]. To this end, the wall is divided into two parts: one in which the myocardium can be completely determined by performing the XOR operation between the endocardial and epicardial masks, and the other formed by removing the voxels inside the blood pool from the epicardial mask. Let $\{p_i^c\}$, $i = 1 \cdots n_c$ be the points on C_{cut}. The unit normal of the plane that divides the wall is determined by

$$\mathbf{N}_L \cdot (p_i-p_m)=0 \quad \text{s.t.} \quad \mathbf{N}_L \cdot (p_{apx}-p_m)<0, \quad (14)$$

where p_m is the centroid of $\{p_i^c\}$, and the constraint specifies the normal direction. The dividing plane is defined as

$$\mathbf{N}_L \cdot (x-p_L)=0, \quad (15)$$

where $p_L \in \{p_i^C\}$ and $\mathbf{N}_L \cdot (p_i - p_L) \le 0, \forall i = 1 \cdots n_c$. That is, all points of C_{cut} lie on the same side of the dividing plane as p_{apx} does. The myocardial wall is the set of voxels that satisfy

$$V_{Wall} = \begin{cases} \tilde{V}_{Endo} \oplus \tilde{V}_{Epi} & \text{if} \quad N_L \cdot (x - p_L) \le 0 \\ \tilde{V}_{Epi} \cap \overline{V}_{BP} & \text{otherwise,} \end{cases} \quad (16)$$

where $\bar{V}_{BP}$ are the set of voxels outside of the blood pool, $\tilde{V}_{Endo}$ and $\tilde{V}_{Epi}$ are the volumes enclosed by the endocaridal and epicardial masks, respectively. An example of extracting the myocardial wall is given in Fig. 6. It is clear that, by using the procedure described above, a smooth endocardial mask is extracted in the presence of noise and papillary muscles. Further, the epicardial mask is separated from the background with soft tissues around the apex point and cut off right around the base area. The shape constraint makes the evolution process go smoothly while preserving the overall shape as well as adapting to the local intensity content.

IV. Experimental Results

This study was approved by the Institutional Review Board. We tested the robustness and accuracy of our method using cardiac CT images of 34 human and 12 pig hearts. The data include anomaly cases (hypertrophic cardiomyopathy and aneurysm) and volumes with different scanning quality.

A. Implementation

The overall framework was implemented in C++. Open source packages ITK [45] and [46] were used for basic image processing tasks, convex hull extraction and 3D visualization, respectively.

In extracting the blood pool, the source image was down-sampled to a voxel resolution of $2.0 \times 2.0 \times 2.0$ mm^3, where the heart shape is well preserved. The thresholds of 180 and 350 in Hounsfield units were used for human and pig images, respectively, so that the left and right ventricles can be separated after thresholding.

B. Parameter Determination and Robustness

To test the robustness of localizing the left ventricle described in Section II, sample points randomly selected from a neighborhood within 30 mm of the apex point were used as trial apex points to start the localization process. To quantify the errors, the distance between the cut contours obtained by using different sample points and the original contour was measured as

$$d(C, \tilde{C}) = \frac{\int_{\tilde{C}(s)} D(C) ds}{\int_{\tilde{C}(s)} ds}. \quad (17)$$

Here, C is the original cut contour, D is the distance field starting from C, and $\tilde{C}$ is the cut contour obtained from a sample point. In implementation, $D(C)$ was evaluated at triangle vertices. The initial and final errors $d(C, \tilde{C})$ for 20 randomly sampled points is shown in Fig. 7. All of the cut contours generated with sampled apex points converge to the original C with a tolerable numerical error. In addition, the average of the turning point $\tilde{d}$ are 94 ± 9 mm and 76 ± 6 mm for the human and pig data, respectively. This result shows that the feature used for identifying the cut contour is stable despite of the variability in heart shapes.

Similarly, the sensitivity of the scale factor S defined in Equation (4) was tested by computing the average distance between the original cut contour and the ones obtained with different scale factors. Experiments showed that the average distance was 0.08 mm as S ranging from 0.001 to 0.1.

The parameters in the feature function $g(\tilde{\varphi})$ were set as $\alpha = 1$, $\beta = 5$, $d_{max} = 1.0$ mm, and $d_{mim} = 0.02$ mm, the width of which is slightly smaller than the average myocardium thickness. Example shapes of this function with varying α are shown in Fig. 8. It implies that larger values of α give a stricter constraint while minimizing Equation (13), and thus $\alpha = 1$ was used.

The sensitivity of the epicardial initialization step to λ_{RS} and d_w were examined separately. Figure 9 shows the average point-to-surface distance for the example image when λ_{RS} varies from 0.1 to 0.9 and d_w from 8 to 24 mm, respectively. λ_{LG} is stable up to 0.8 for the epicardial initialization, after which the growing process stops before reaching the epdicardial boundary due to the high curvature constraint. Regarding d_w, the localization step is stable for $d_w > 16$ mm, which agrees with the thickness of a normal myocardial wall [3].

The sensitivities of the parameters λ_{LG} and r were examined by varying one of them in a given range while keeping the other fixed. The coefficients of variation [47] are summarized in Table I. It shows that all these parameters are stable in the given range.

Our method succeeded in localizing the left ventricle for all of the testing data with wide shape variations and volume coverages. Two examples of segmentation for the human data with completely different heart shapes are presented in Fig. 10. The results of pig data with different volume coverages are shown in Fig. 11. As can be seen from these results, the papillary muscles, pericardium, and soft tissues were successfully excluded from the myocardium.

C. Quantitative Analysis

To make fair comparisons, all testing data were resampled to the same resolution of the manual segmentations at 1.0 × 1.0 × 1.0 mm^3. The mean and standard deviation of the point-to-surface errors for the human and pig data at the localization and refinement steps are shown in Table II. These results show that the localization step (LV localization) locates the endocardial and epicardial masks with high precision as compared to the manual segmentations, which are further refined after applying the active contour model with a shape constraint (AC refinement). Note that the accuracy of the endocardial segmentation is better than the epicardial segmentation as the former is better defined because of the high contrast between the blood pool and the myocardium, while in the latter case poor contrast and weak edges are present between the epicardium and background tissues.

The proposed method was compared to three types of training-based methods: an active contour method using localized PCA [23], [24], an active shape model (ASM) [4] method, and a standard multi-atlas method with a majority voting scheme [48] for segmenting the pig myocardium using the same dataset. For the latter two methods, the leave-one-out strategy was used due to the small number of images. In particular, the localization results from the proposed method were used to estimate the initial pose of the ASM model for segmentation. Regarding the multi-atlas-based method, affine registration was first applied to align training images to a testing image, which was refined by employing the B-Spline registration method [49]. Parameters were tuned to give the best performance for the three training-based methods. An example of segmentations from these methods is shown in Fig. 12, and the statistics of the surface-to-point errors of these methods are summarized in Table III. These results demonstrate the different characteristics of these four types of methods. The proposed method captured more local image content as compared to the other three methods. The PCA based active contour method also performed well but was less adaptive, since it relies on the sub-space learned from the training images. The ASM method failed to capture the finer details for both the endcardium and epicardium as it is essentially a PCA based method, which depends on how representative the training image are. The atlas-based method was not competitive with the other tested methods as it is mainly driven by global image information, and thus may not be able to compensate for large initialization errors especially when images have a wide volume coverage (see Fig. 11).

In addition, the proposed method was tested on a computer with Quad CPU 3GHz, 8G RAM. The average processing time is given in Table IV.

Given the mask of a myocardium wall, we triangulated it and computed the volume enclosed by this triangulated surface using the same computational method as in [50]. The mass was computed as the product of the volume and density. The density $\rho = 1.05 g/mL$ was used in our experiments. For the human data, the average absolute difference between the masses from automatic and manual segmentations was $7.8 \pm 5.0g$, which is 5.5% ± 3.5% with respect to the mean mass. For the pig data, this difference was $4.2 \pm 2.9g$, which accounts for 6.4% ± 4.4% of the mean mass.

V. Discussion and Future Work

We have presented a complete system for automatically segmenting the myocardial wall from cardiac CT images. It follows the coarse-to-fine framework by first detecting the left ventricle, and then refining this result by employing contour evolution techniques with a shape constraint obtained on-line. Its performance has been evaluated by measuring the errors between automatic and manual segmentations. In these tests, our method achieved high accuracy as well as strong robustness for segmenting both the human and pig myocardium with large shape variabilities and different volume coverage.

Though the proposed method was specific for the segmentation of the left ventricular myocardium, it may be generalized in several possible ways for broader applications in cardiac image segmentations. It is straightforward to apply the shape segmentation technique to segment the right ventricle from CT images because of the similarity of ventricle structures. In addition, the proposed method may be applied to other image modalities as long as a smooth heart surface can be reconstructed. For example, in MR images, we may manually threshold an MR image to extract the blood pool and then generate the heart surface. Moreover, the proposed method can be easily integrated into user interactive segmentation frameworks, which are widely used in medical image segmentations. In particular, for ventricles with an arbitrary orientation, a user can effectively pinpoint the apex point to start the segmentation.

Therefore, in future work, we plan to extend the current method to segment ventricles both in CT and MR images and apply segmentation results to clinical applications such as evaluating the myocardial mass at risk caused by stenoses.

Acknowledgments

This work was supported in part by the National Institutes of Health (NIH), AFOSR, in part by the National Alliance for Medical Image Computing, in part by the National Institutes of Health through the NIH Roadmap for Medical Research under Grant U54 EB005149, in part by the National Center for Research Resources under Grant P41-RR-013218, in part by the National Institute of Biomedical Imaging and Bioengineering through NIH under Grant P41-EB-015902, and in part by NIH under Grant R01 HL085417. The associate editor coordinating the review of this manuscript and approving it for publication was Prof. Jean-Philippe Thiran.

We especially wish to acknowledge our deep gratitude to Dr. Faber who had helped to push this research forward and devoted her life to cardiac imaging analysis. We would also like to thank Dr. Ernest Garcia of Emory from some useful discussions about the topic of this paper. Dr. Faber receives royalties from the sale of the Emory Cardiac Toolbox and has an equity position in Syntermed, Inc., which markets ECTb. The terms of this arrangement have been reviewed and approved by Emory University in accordance with its conflict of interest policies.

References

1. World Heart Federation and World Stroke Organization, . Global Atlas on Cardiovascular Disease Prevention and Control. Geneva, Switzerland: WHO; 2011.
2. Suri JS. Computer vision, pattern recognition and image processing in left ventricle segmentation: The last 50 years. Pattern Anal Appl. 2000; 3(3):209–242.
3. Petitjean C, Dacher JN. A review of segmentation methods in short axis cardiac MR images. Med Image Anal. 2011; 15(2):169–184. [PubMed: 21216179]
4. Cootes TF, Taylor CJ, Cooper DH, Graham J. Active shape models-their training and application. Comput Vis Image Understand. 1995; 61(1):38–59.
5. van Assen HC, Danilouchkine MG, Dirksen MS, Reiber JH, Lelieveldt BP. A 3-D active shape model driven by fuzzy inference: Application to cardiac CT and MR. IEEE Trans Inf Technol Biomed. Sep; 2008 12(5):595–605. [PubMed: 18779074]
6. van Assen HC, Danilouchkine MG, Frangi FF, Ordas S, Westenberg JJ, Reiber JH, et al. SPASM: A 3D-ASM for segmentation of sparse and arbitrarily oriented cardiac MRI data. Med Image Anal. 2006; 10(2):286–303. [PubMed: 16439182]
7. Cootes TF, Edwards GJ, Taylor CJ. Active appearance models. IEEE Trans Pattern Anal Mach Intell. Jun; 2001 23(6):681–685.
8. Mitchell SC, Lelieveldt B, van der Geest RJ, Bosch JG, Reiber JHC, Sonka M. Multistage hybrid active appearance model matching: Segmentation of left and right ventricles in cardiac MR images. IEEE Trans Med Imag. May; 2001 20(5):415–423.

9. Essafi S, Langs G, Paragios N. Hierarchical 3D diffusion wavelet shape priors. Proc Int Conf Comput Vis. 2009:1717–1724.
10. Ecabert O, Peters J, Schramm H, Lorenz C, von Berg J, Walker M. Automatic model-based segmentation of the heart in CT images. IEEE Trans Med Imag. Sep; 2008 27(9):1189–1201.
11. Zheng Y, Barbu A, Georgescu B, Scheuering M, Comaniciu D. Four-chamber heart modeling and automatic segmentation for 3-D cardiac CT volumes using marginal space learning and steerable features. IEEE Trans Med Imag. Nov; 2008 27(11):1668–1681.
12. van Rikxoort EM, Isgum I, Arzhaeva Y, Staring M, Klein S, Viergever MA, et al. Adaptive local multi-atlas segmentation: Application to the heart and the caudate nucleus. Med Image Anal. 2010; 14(1):39–49. [PubMed: 19897403]
13. Zhuang X, Rhode KS, Razavi RS, Hawkes DJ, Ourselin S. A registration-based propagation framework for automatic whole heart segmentation of cardiac MRI. IEEE Trans Med Imag. Sep; 2010 29(9):1612–1625.
14. Lempitsky, VS.; Verhoek, M.; Noble, JA.; Blake, A. Random forest classification for automatic delineation of myocardium in real-time 3D echocardiography. Proc. 5th Int. Conf. Funct. Imag. Model. Heart; 2009. p. 447-456.
15. Kichenassamy, S.; Kumar, A.; Olver, P.; Tannenbaum, A.; Yezzi, A. Gradient flows and geometric active contour models. Proc. 5th Int. Conf. Comput. Vis; Washington, DC, USA. 1995. p. 810-815.
16. Caselles V, Kimmel R, Sapiro G. Geodesic active contours. Int J Comput Vis. 1997; 22(1):61–79.
17. Chan TF, Vese LA. Active contours without edges. IEEE Trans Image Process. Feb; 2001 10(2): 2029–2039.
18. Wang X, Huang DS, Xu H. An efficient local Chan-Vese model for image segmentation. Pattern Recognit. 2010; 43(3):603–618.
19. Chen L, Zhou Y, Wang Y, Yang J. Rapid and brief communication: GACV: Geodesic-aided C-V method. Pattern Recognit. Jul; 2006 39(7):1391–1395.
20. Lankton, S.; Nain, D.; Yezzi, A.; Tannenbaum, A. Hybrid geodesic region-based curve evolutions for image segmentation. Proc. SPIE; Mar. 2007; p. 65104U
21. Lankton S, Tannenbaum A. Localizing region-based active contours. IEEE Trans Image Process. Nov; 2008 17(11):2029–2039. [PubMed: 18854247]
22. Tsai A, Yezzi A, Wells W, Tempany C, Tucker D, Fan A, et al. A shape-based approach to the segmentation of medical imagery using level sets. IEEE Trans Med Imag. Feb; 2003 22(2):137–154.
23. Appia, V.; Ganapathy, B.; Abufadel, A.; Yezzi, A.; Faber, T. A regions of confidence based approach to enhance segmentation with shape priors. Proc SPIE; May 2010; p. 753302
24. Appia, V.; Ganapathy, B.; Yezzi, A.; Faber, T. Localized principal component analysis based curve evolution: A divide and conquer approach. Proc. IEEE Int. Comput. Vis. Conf; Nov. 2011; p. 1981-1986.
25. Paragios N. A level set approach for shape-driven segmentation and tracking of the left ventricle. IEEE Trans Pattern Anal Mach Intell. Jun; 2003 22(6):776–773.
26. Jolly M. Automatic segmentation of the left ventricle in cardiac MR and CT images. Int J Comput Vis. 2006; 70(2):151–163.
27. Lynch M, Ghita O, Whelan P. Left-ventricle myocardium segmentation using a coupled level-set with a priori knowledge. Comput Med Imag Graph. 2006; 30(4):255–262.
28. Zeng X, Staib LH, Schultz RT, Duncan JS. Segmentation and measurement of the cortex from 3D MR images using coupled surfaces propagation. IEEE Trans Med Imag. Oct; 1999 18(10):927–937.
29. Zimmer C, Olivo-Marin J. Coupled parametric active contours. IEEE Trans Pattern Anal Mach Intell. Nov; 2005 27(11):1838–1842. [PubMed: 16285382]
30. Lynch M, Ghita O, Whelan P. Automatic segmentation of the left ventricle cavity and myocardium in MRI data. Comput Biol Med. Apr; 2006 36(4):389–407. [PubMed: 15925359]
31. Shamir A. A survey on mesh segmentation techniques. Comput Graph Forum. 2008; 27(6):1539–1556.

32. Attene, M.; Katz, S.; Mortara, M.; Patanè, G.; Spagnuolo, M.; Tal, A. Mesh segmentation—A comparative study. Proc. IEEE Int. Conf. Shape Model. Appl; Jun. 2006; p. 14-25.
33. Katz S, Tal A. Hierarchical mesh decomposition using fuzzy clustering and cuts. ACM Trans Graph. Jul; 2003 22(3):954–961.
34. Katz S, Leifman G, Tal A. Mesh segmentation using feature point and core extraction. Vis Comput. 2005; 21(8–10):649–658.
35. Bajaj C, Goswami S, Yu Z, Zhang Y, Bazilevs Y, Hughes T. Patient specific heart models from high resolution CT. Proc Int Symp Comput Model Objects Represented Images, Fundam, Methods, Appl. 2006
36. Càrdenes R, Pozo J, Bogunovic H, Larrabide I, Frangi A. Automatic aneurysm neck detection using surface Voronoi diagrams. IEEE Trans Med Imag. Oct; 2011 30(10):1863–1876.
37. Kaplansky L, Tal A. Mesh segmentation refinement. Pacific Graph. 2009; 28(7):1995–2003.
38. Lai R, Chan TF. A framework for intrinsic image processing on surfaces. Comput Vis Image Understand. 2011; 115(12):1647–1661.
39. John M, Rahn N. Automatic left atrium segmentation by cutting the blood pool at narrowings. Proc MICCAI. 2005:798–805.
40. Gao Y, Kikinis R, Bouix S, Shenton M, Tannenbaum A. A 3D interactive multi-object segmentation tool using local robust statistics driven active contours. Med Image Anal. 2012; 16(6):1216–1217. [PubMed: 22831773]
41. Crick SJ, Sheppard MN, Ho SY, Gebstein L, Anderson RH. Anatomy of the pig heart: Comparisons with normal human cardiac structure. J Anatomy. Jul.1998 193:105–119.
42. Kimmel R, Sethian JA. Computing geodesic paths on manifolds. Proc Nat Acad Sci United States Amer. 1998; 95(15):8431–8435.
43. Whitaker RT. A level-set approach to 3D reconstruction from range data. Int J Comput Vis. Sep; 1998 29(3):203–231.
44. Aubert, G.; Kornprobst, P. Applied Mathematical Sciences. New York, NY, USA: Springer-Verlag; 2006. Mathematical Problems in Image Processing: Partial Differential Equations and the Calculus of Variations.
45. Insight Segmentation and Registration Toolkit (ITK). 2013. [Online]. Available: http://www.itk.org/
46. Visualization Toolkit (VTK). 2013. [Online]. Available: http://www.vtk.org/
47. Reed GF, Lynn F, Meade BD. Use of coefficient of variation in assessing variability of quantitative assays. Clin Diag Lab Immunol. 2002; 9(6):1235–1239.
48. Cabezas M, Oliver A, Lladò X, Freixenet J, Meritxell BC. A review of atlas-based segmentation for magnetic resonance brain images. Comput Methods Programs Biomed. Dec; 2011 104(3):e158–e177. [PubMed: 21871688]
49. Rueckert D, Sonoda LI, Hayes C, Hill DLG, Leach MO, Hawkes DJ. Nonrigid registration using free-form deformations: Application to breast MR images. IEEE Trans Med Imag. Aug; 1999 18(8):712–721.
50. Zhu L, Mohan V, Stillman A, Faber T, Tannenbaum A. Estimation of myocardial volume at risk from CT angiography. Proc SPIE. Mar.2011 2011:79632A-1–79632A-6.

Biographies

Liangjia Zhu is a Post-Doctoral Fellow with the Department of Computer Science, Stony Brook University. He received the Ph.D. degree in electrical engineering from the Georgia Institute of Technology in 2013. His research interests include image processing, computer vision, and video analysis.

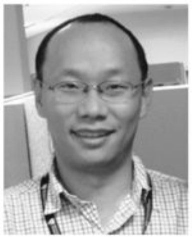

Yi Gao is an Assistant Professor with the Department of Electrical and Computer Engineering, University of Alabama at Birmingham. He is an Associate Scientist with the UAB Comprehensive Cancer Center. His research interests include computer vision, image, and shape computing.

Vikram Appia is currently with the Imaging Technology Laboratory in the Embedded Processing Research and Development Center, Texas Instruments, Dallas, USA. He received the Ph.D. degree from the School of Electrical and Computer Engineering, Georgia Institute of Technology, Atlanta, USA, in 2012. He was a Research Intern with GE-Global Research, Bangalore. His research interests lie primarily in the fields of computer vision and image processing with a special focus in the areas of image segmentation, multicamera systems, multimodal data fusion, depth imaging, active contour models, PDE-based methods, and level set based methods.

Anthony Yezzi holds the position of Ken Byers Professor with the School of Electrical and Computer Engineering, Georgia Institute of Technology (Georgia Tech), where he directs the Laboratory for Computational Computer Vision. He has over 20 years of research experience in shape optimization via geometric partial differential equations. He received the Ph.D. degree in electrical engineering from the University of Minnesota in 1997. After completing a post-doctoral research appointment with the Massachusetts Institute of Technology, he joined the faculty of the Georgia Tech in 1999. His research lies primarily within the fields of image processing and computer vision with a particular emphasis on medical imaging and 3D surface reconstruction. He has consulted for a number of companies, including GE, 3M, MZA, Philips, Picker, and VTI. His work spans a wide range of image processing and vision problems, including image denoising, edgedetection, segmentation, shape analysis, multiframe stereo reconstruction, visual tracking, and registration. His research interests include curve and surface evolution, differential geometry, partial differential equations, and shape optimization.

Chesnal Arepalli is a Research Associate with the Department of Radiology, Emory University. He graduated from Gandhi and Osmania Medical Colleges, Hyderabad, India. He was a Clinical Fellow of cardiovascular radiology with AIIMS, New Delhi. He is interested in translating research and findings into clinical arena.

Tracy Faber has been a Professor with Emory University since 1992; previously she was on the faculty of the Southwestern Medical Center, Dallas. She was a member of the program faculty with the Joint Department of Biomedical Engineering, Emory University and Georgia Institute of Technology (Georgia Tech), and the Computing and Visualization Laboratory, Georgia Tech. Her research focused on computer aided diagnosis from medical images. This involves restoration, segmentation, labeling, registration, and 3D visualization.

Arthur Stillman is the William and Kay Casarella Professor of radiology and the Director of cardiothoracic imaging with Emory University. He is a Past President of the North American Society for Cardiovascular Imaging and is the Past Chair of the Cardiovascular Radiology and Intervention Council of the American Heart Association. He is a Distinguished Investigator of the Academy of Radiology Research. He has published over 139 scholarly papers mostly in areas of research involving cardiac MRI and CT. He is the Principle Investigator of a multicenter comparative effectiveness trial comparing coronary CT angiography to SPECT-MPI for guiding patients with symptoms of stable angina to optimized medical therapy (RESCUE: Randomized Evaluation of Patients with Stable Angina Comparing Utilization of Diagnostic Examinations). The findings are expected to result in validation of an evolving new standard of care for patients with stable angina that takes advantage of coronary CT angiography to more cost effectively drive appropriate care.

Allen Tannenbaum has held faculty positions in Israel, Canada, Switzerland, and the U.S. He is currently a Professor of computer science and applied mathematics/statistics with SUNY Stony Brook. He works in image processing, medical informatics, computer vision, and systems and control.

Appendix

Given the definition in Equation (8), the discretized gradient operator on T_k is computed as [38]

$$\begin{aligned}\nabla_{T_k} f(p_1) &= \sum_{i,j=1}^{2} g^{ij} \frac{\partial f}{\partial \chi^j} \partial_{\chi^i} \\ &= (f(p_1)-f(p_3), f(p_2)-f(p_3)) g^{-1} \begin{pmatrix} \partial_{\chi^1} \\ \partial_{\chi^2} \end{pmatrix} \\ &= (f(p_1)-f(p_3), f(p_2)-f(p_3)) \times \begin{pmatrix} \partial_{\chi^1} \cdot \partial_{\chi^1} & \partial_{\chi^1} \cdot \partial_{\chi^2} \\ \partial_{\chi^2} \cdot \partial_{\chi^1} & \partial_{\chi^2} \cdot \partial_{\chi^2} \end{pmatrix}^{-1} \begin{pmatrix} p_1 - p_3 \\ p_2 - p_3 \end{pmatrix}\end{aligned} \quad (18)$$

where $\partial_{\chi}1 = p_1 - p_3$ and $\partial_{\chi}2 = p_2 - p_3$ are the two tangent vectors at p_3 that span the tangent plane T_pM of a surface M. The matrix $g^{-1} = (g^{i,j})$ is the inverse of the Riemannian metrics on M with

$$g = (g_{i,j}) = \begin{pmatrix} \partial_{\chi^1} \cdot \partial_{\chi^1} & \partial_{\chi^1} \cdot \partial_{\chi^2} \\ \partial_{\chi^2} \cdot \partial_{\chi^1} & \partial_{\chi^2} \cdot \partial_{\chi^2} \end{pmatrix}. \quad (19)$$

The vector field on T_k can be represented in the local coordinate as $\mathbf{V} = \upsilon_1 \, \partial_{\chi^1} + \upsilon_2 \, \partial_{\chi^2}$. The discretization of the divergence operator on T_k is

$$\begin{aligned} \nabla_{T_k} \cdot \mathbf{V}(p_1) &= \frac{1}{\sqrt{G}} \sum_{i=1}^{2} \frac{\partial}{\partial \chi^i} \left(\sqrt{G} v^i \right) \\ &= \frac{\partial}{\partial \chi^1} (v_1) + \frac{\partial}{\partial \chi^2} (v_2) \\ &= \left(g^{11} (\mathbf{V}(p_1) - \mathbf{V}(p_3)) + g^{21} (\mathbf{V}(p_2) - \mathbf{V}(p_3)) \right) \partial_{\chi^1} + \left(g^{12} (\mathbf{V}(p_1) - \mathbf{V}(p_3)) + g^{22} (\mathbf{V}(p_2) - \mathbf{V}(p_3)) \right) \partial_{\chi^2} . \end{aligned} \tag{20}$$

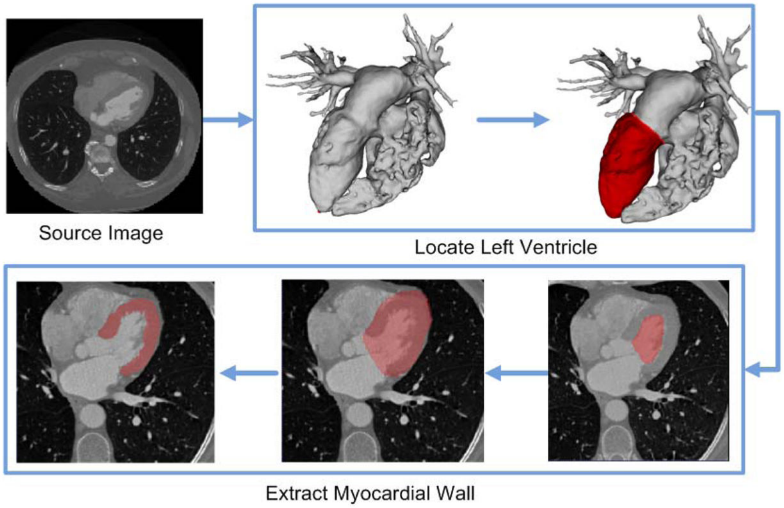

Fig. 1.
Flowchart of the proposed approach.

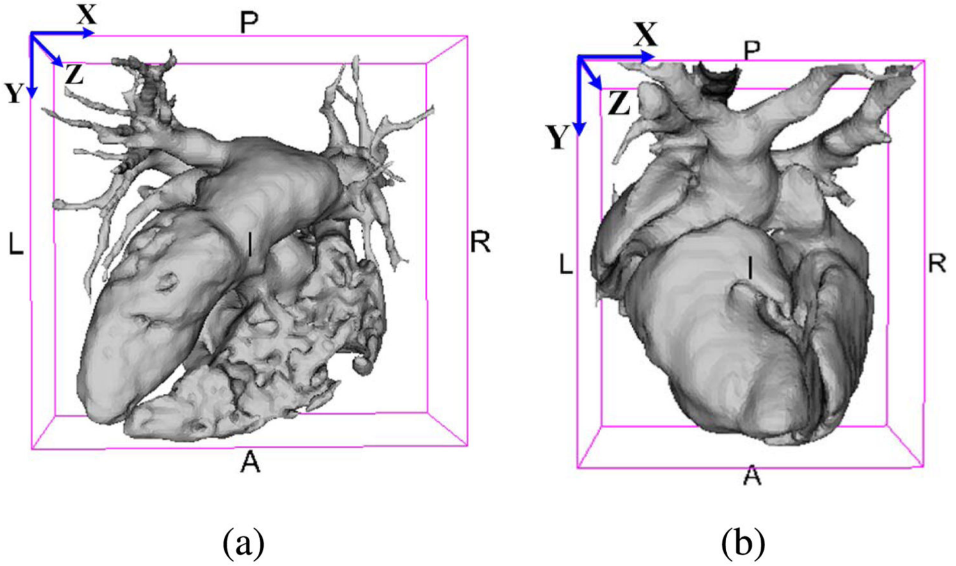

Fig. 2.

Orientations of (a) human and (b) pig blood pool surfaces in the source image coordinate system. The reference directions are left(L), right(R), posterior(P), anterior(A), inferior(I), and superior(S).

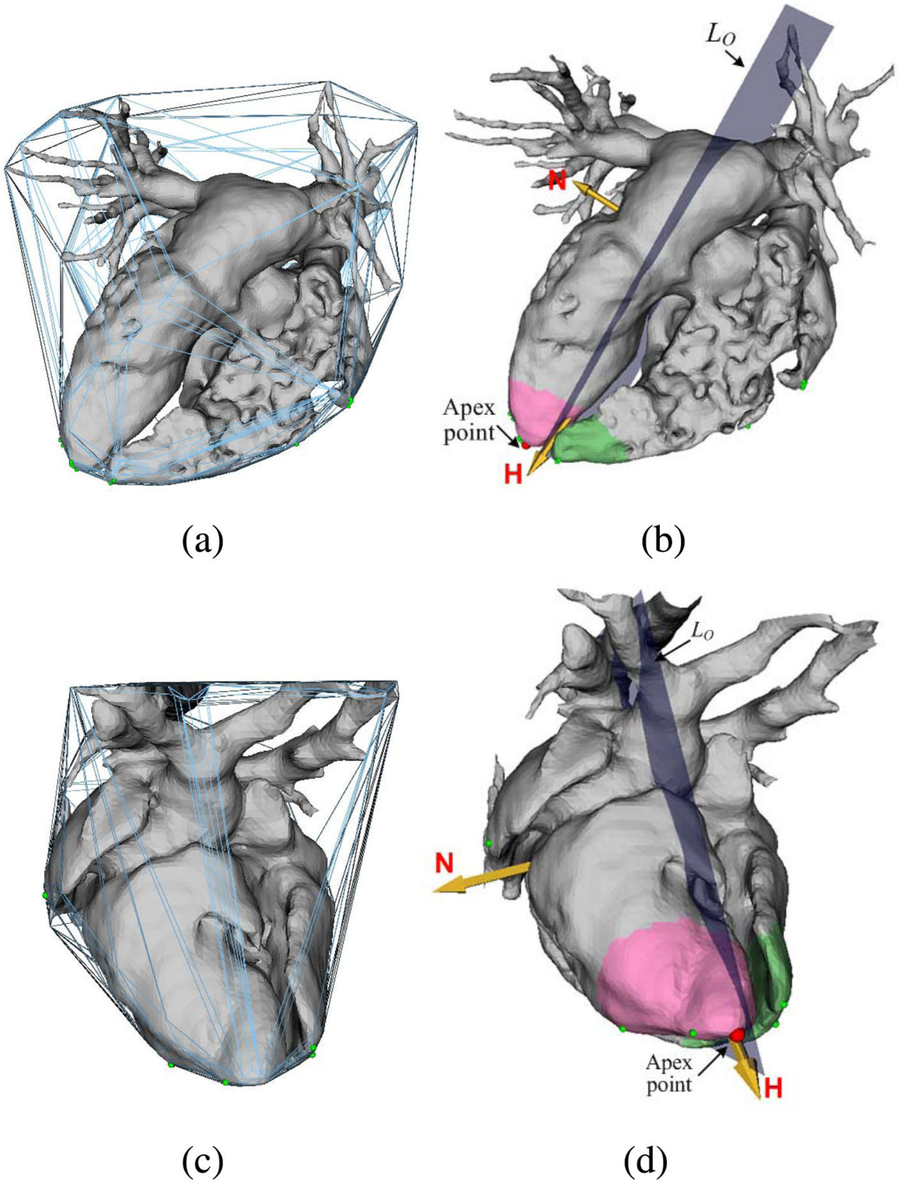

Fig. 3.

Apex detection of human and pig hearts. Convex hull with high curvature points (green) for the human (a) and pig (c) hearts. Neighborhoods around apex points for human (b) and pig (d) hearts. The detected apex points are marked with red dots. The vector **H** represents the left ventricle orientation. The plane L_O with normal **N** identifies the directions of *left* and *right*.

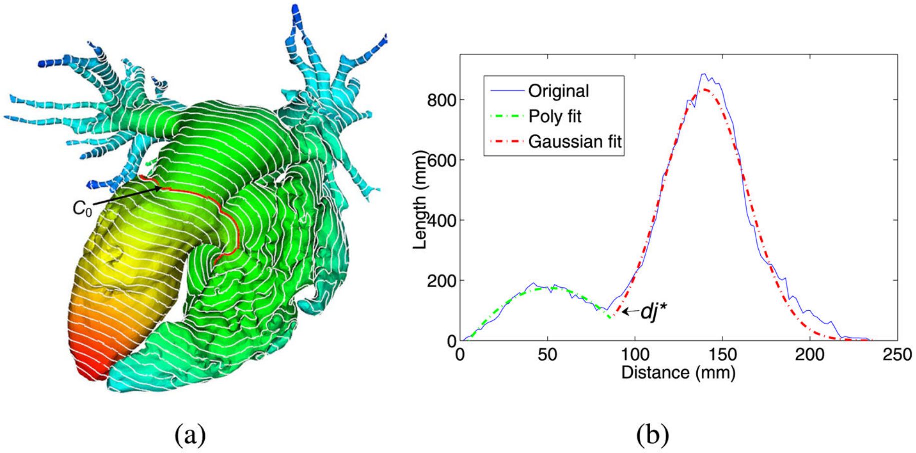

Fig. 4.

Detection of the initial cut contour. (a) Distance field from the apex with isocontours. The initial cut contour C_0 is marked in red. (b) The length of isocontours vs. distance, and the determination of the optimal d_j^*.

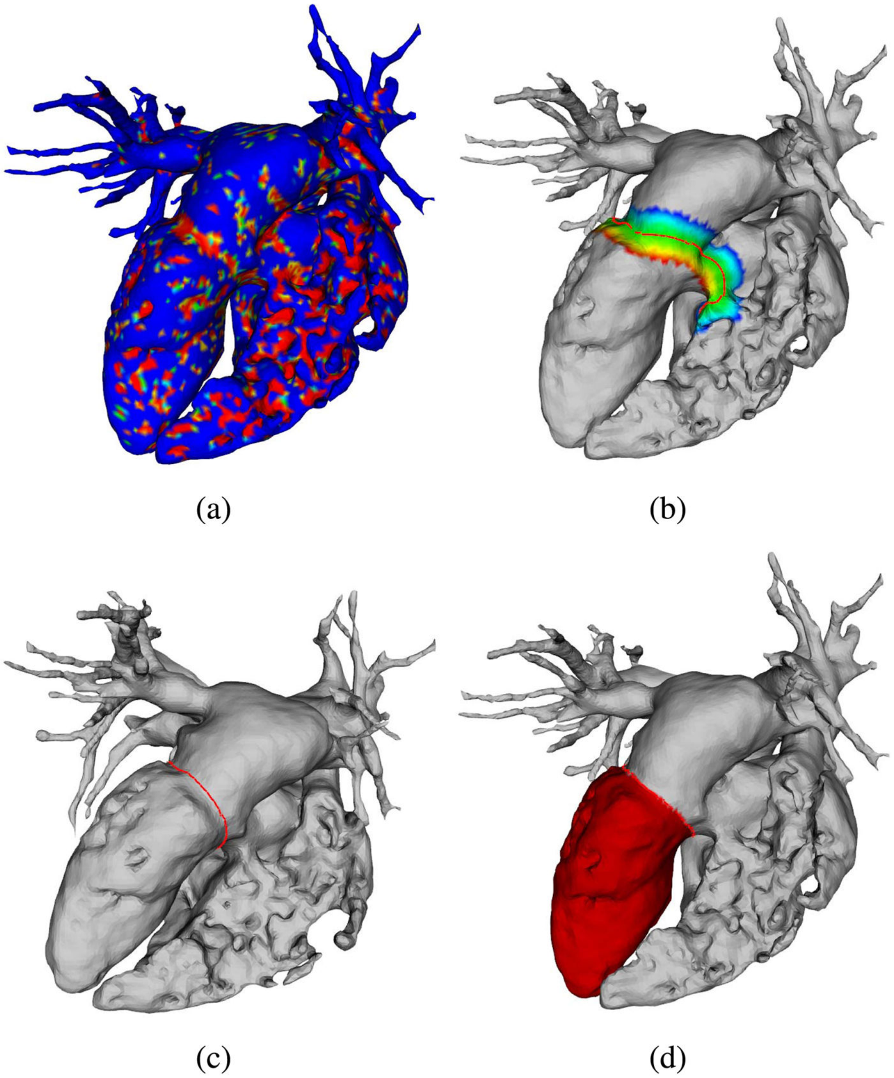

Fig. 5.

Left ventricle localization. (a) Features on surface M_{bp}. (b) Initial contour C_0 and its narrow band $\Omega_{M^{bp}}$. (c) Final contour C_{cut}. (d) Segmented endocardial surface.

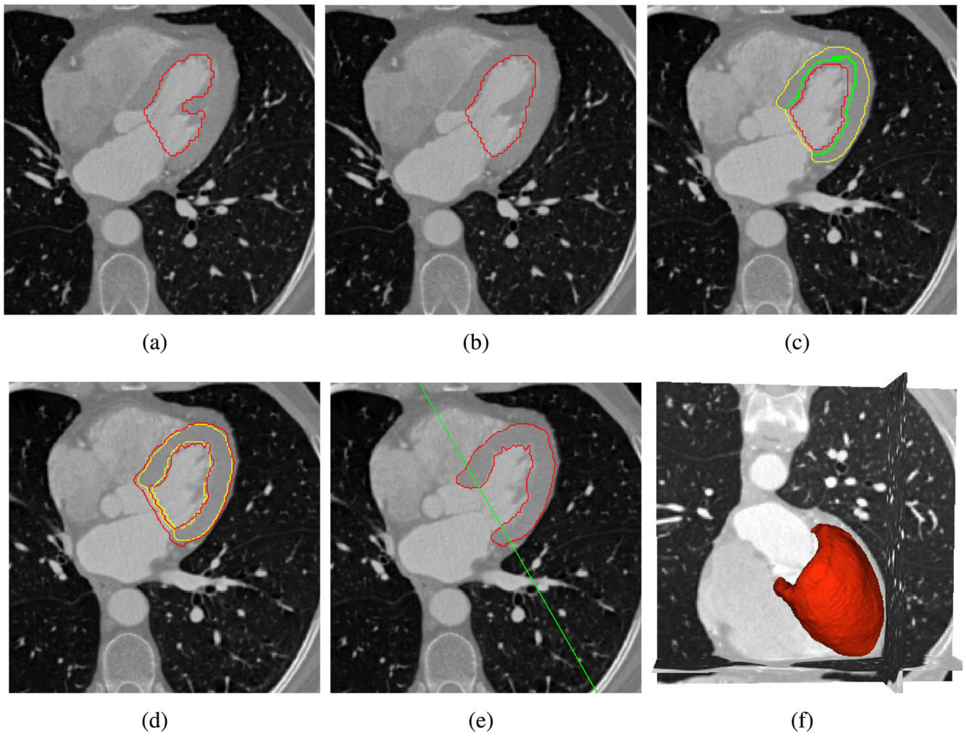
(a) (b) (c)

(d) (e) (f)

Fig. 6.

Segmentation of the myocardial wall. Initialize the endocardial surface (red) (a) before and (b) after removing papillary muscles. (c) Initialize the epicardial surface (yellow) from the initial endocarial surface (red) with a seed region (green). (d) Evolve the myocardial surfaces from the initial contours (yellow). (e) Extract the myocardial wall from endo- and epi- cardial masks by using the dividing plane (green). (f) The 3D visualization of the segmented myocardial wall.

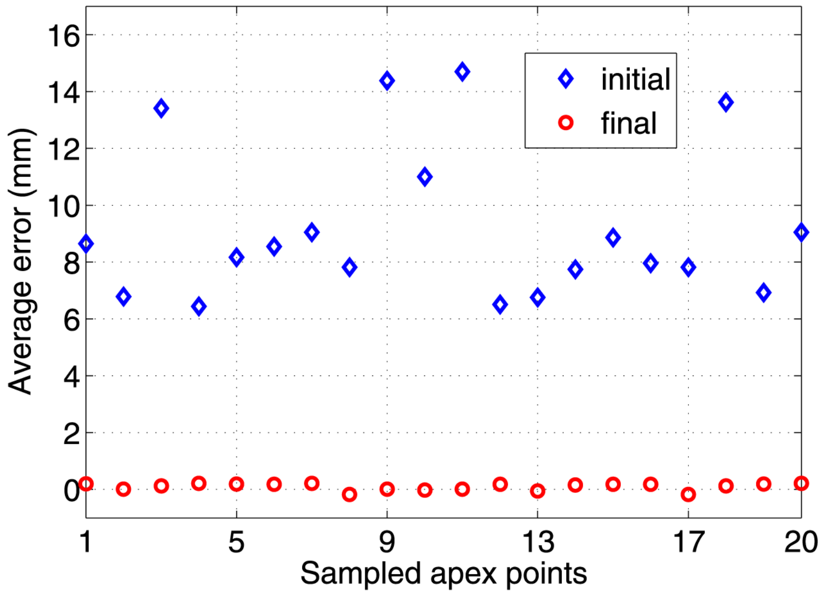

Fig. 7.

The initial and final errors for the cut contours generated from 20 randomly sampled apex points.

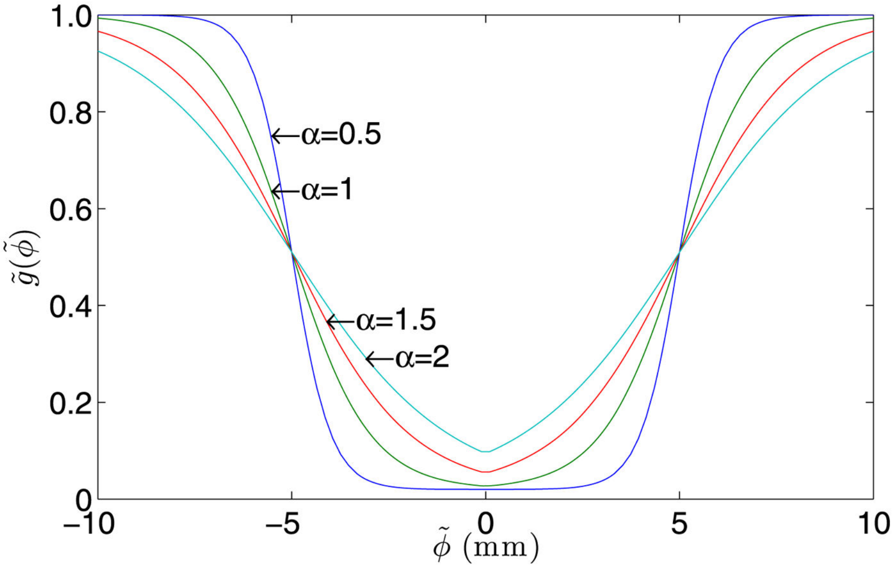

Fig. 8.

Effects of α to $g(\tilde{\varphi})$ with $\beta = 5$, $d_{max} = 1$ mm and $d_{min} = 0.02$ mm.

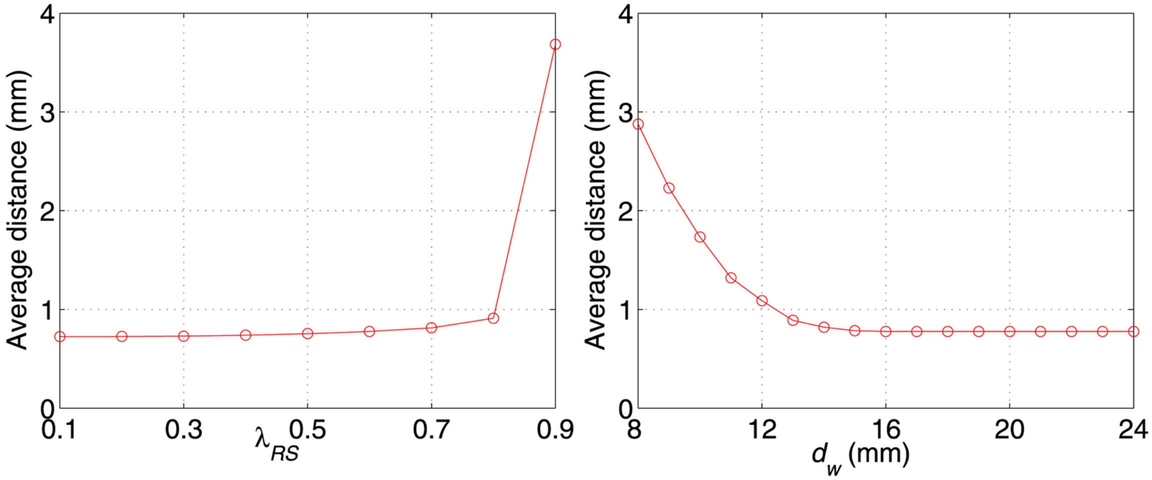

Fig. 9.

Sensitivity of the epicardial initialization with respect to λ_{RS} (Left) and d_w (Right).

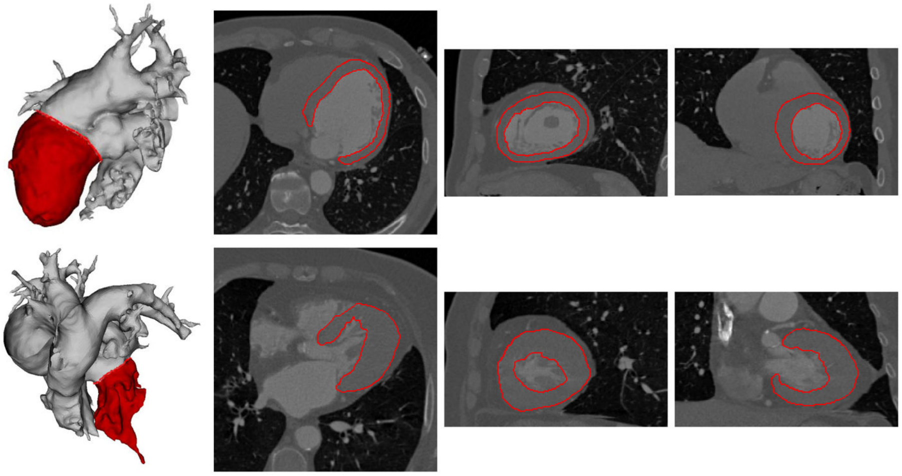

Fig. 10.

Myocardium segmentation results of human data with completely different heart shapes. The first row shows segmentations in a diastole cycle. The second row shows the results of a patient with hypertrophic cardiomyopathy. From left to right are left ventricle localization, myocardial wall in axial, coronal, and sagittal views, respectively.

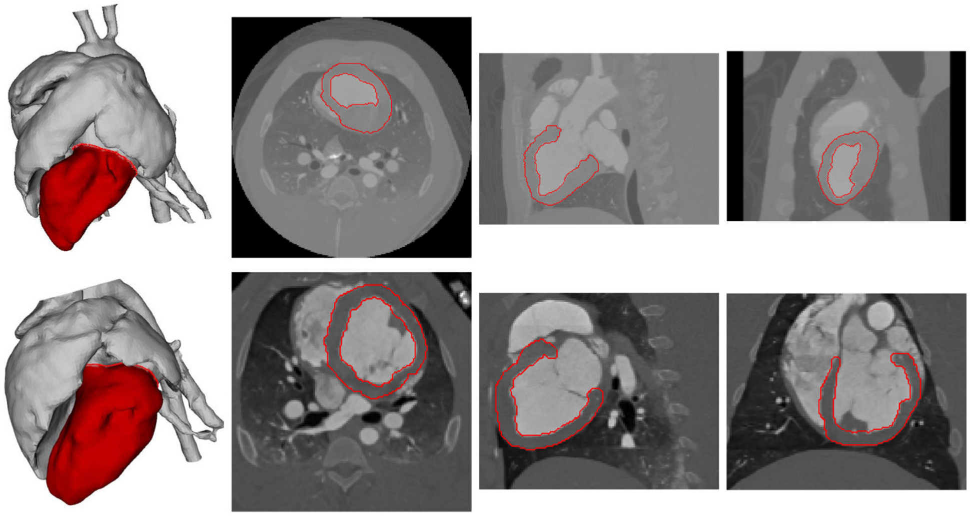

Fig. 11.

Myocardium segmentation results of pig data with different volume coverages. From left to right are left ventricle localization, myocardial wall in axial, coronal, and sagittal views, respectively.

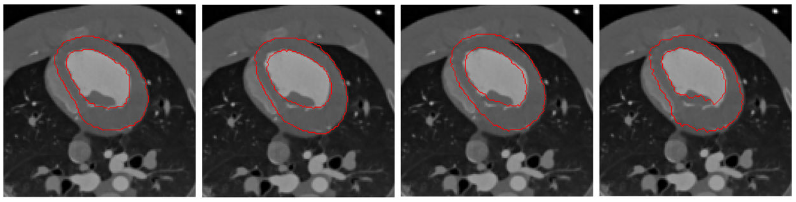

Fig. 12.

Comparison of myocardium segmentation. From left to right are results from the proposed method, localized-PCA, ASM, and Multi-Atlas methods, respectively.

TABLE I

Coefficient of Variation for Wall Refinement

Parameters	Range	Endo-Surface	Epi-Surface
λ_{LG}	[0.2, 0.8]	1.9%	3.4%
r	[2, 10]	1.2%	2.1%

TABLE II

Mean and Standard Deviation of the Point-to-Surface Errors in Localization and Refinement (in mm)

Data	**Stages**	**Endo-Surface**	**Epi-Surface**
Human	LV localization	1.07 ± 1.03	1.27 ± 1.24
	AC refinement	0.88 ± 0.96	1.07 ± 1.16
Pig	LV localization	0.83 ± 0.89	1.05 ± 1.12
	AC refinement	0.72 ± 0.88	0.80 ± 0.99

TABLE III

Comparison Between Proposed Method and Training-Based Methods for the Pig Data (in mm)

Method	**Endo-Surface**	**Epi-Surface**
Proposed method	0.72 ± 0.88	0.80 ± 0.99
Localized-PCA	1.08 ± 1.12	1.10 ± 1.40
ASM	1.12 ± 0.90	1.35 ± 1.37
Multi-Atlas	1.76 ± 1.97	1.48 ± 2.06

TABLE IV

Average Computation Time (in Seconds)

	Human	**Pig**
LV Localization	25.2	15.6
AC Refinement	61.6	41.6
Total	89.0	58.1